# Quasi-Optical 3D localization using Asymmetric Signatures above 100 GHz

Atsutse Kludze Princeton University kludze@princeton.edu

Edward Knightly Rice University knightly@rice.edu Rabi Shrestha Brown University rabi\_shrestha@brown.edu

Daniel Mittleman
Brown University
daniel mittleman@brown.edu

Chowdhury Miftah Karlsruhe Institute of Technology cmm.sagir@ieee.org

Yasaman Ghasempour Princeton University ghasempour@princeton.edu

#### **ABSTRACT**

The spectrum above 100 GHz has the potential to enable accurate 3D wireless localization due to the large swath of available spectrum. Yet, existing wide-band localization systems utilize the time of arrival measurements requiring strict time synchronization. In this paper, we present 123-LOC, a novel non-coherent system for one-shot dual-polarized 3D localization above 100 GHz. Our key idea is to create unique asymmetric THz fingerprints in 3D so that a wireless node can jointly infer its angular position and distance by taking hints from the measured power-spectrum profile. We introduce a dual-polarized dual-slit waveguide structure that emits out signals into free-space with a key feature that the beam pattern depends on the frequency of the signal and the geometry of the slit. To distinguish the emissions from the two slits, we use polarization diversity and manipulate the aperture geometry of the two slits so that they transmit slightly different angular-spectral signatures. Our over-the-air experiments demonstrate that 123-LOC achieves an average angle estimation error of 1° together with millimeter-scale ranging resolution, solely through non-coherent power measurements.

# **CCS CONCEPTS**

• Networks  $\rightarrow$  Network protocol design; Wireless local area networks; Mobile networks.

#### **KEYWORDS**

Localization, THz, polarization, leaky waveguide, dispersion

#### **ACM Reference Format:**

Atsutse Kludze, Rabi Shrestha, Chowdhury Miftah, Edward Knightly, Daniel Mittleman, and Yasaman Ghasempour. 2022. Quasi-Optical 3D localization using Asymmetric Signatures above 100 GHz. In *The 28th Annual International Conference On Mobile Computing And Networking (ACM MobiCom '22), October 17–21, 2022, Sydney, NSW, Australia.* ACM, New York, NY, USA, 13 pages. https://doi.org/10.1145/3495243.3517022



This work is licensed under a Creative Commons Attribution International 4.0 License. *ACM MobiCom '22, October 17–21, 2022, Sydney, NSW, Australia* © 2022 Copyright held by the owner/author(s). ACM ISBN 978-1-4503-9181-8/22/10. https://doi.org/10.1145/3495243.3517022

#### 1 INTRODUCTION

Wireless 3D localization technology is emerging as a key enabler for a wide range of applications from indoor navigation and augmented reality to smart robots [28, 36, 38, 39]. In principle, the resolution of RF-based localization systems is bound to the bandwidth, motivating the use of millimeter-wave (mmWave) and terahertz (THz) frequencies that offer plentiful bandwidth for accurate localization. Indeed, the US Federal Communications Commission (FCC) has recently opened multiple unlicensed bands above 95 GHz for both communication and localization in future (beyond 5G) wireless systems [6]. Conventionally, 3D localization based on wide bandwidth technology utilizes time of arrival (ToA) or time difference of arrival (TDoA) measurements [21, 22, 29, 47]. Unfortunately, such solutions require strict time-synchronization between wireless endpoints which becomes extremely challenging in practice due to the high sampling rate above 100 GHz, which we refer to as the THz regime.

In this paper, we present 123-LOC, a novel non-coherent system for One-shot Dual-Polarized 3D Localization in the THz range. Our key idea is to create unique THz spectral fingerprints in 3D space to enable a wireless node to jointly infer angular position (azimuth and elevation angles) and distance relative to a transmitting reference node by taking hints from measured spectral attributes and not timing or phase information (thereby, non-coherent estimation).

First, we introduce a new architecture that allows for simultaneous emission of a wide set of frequencies in different directions. Our design is motivated by the quasi-optical frequency-dependent dispersion in THz leaky-wave antennas (LWAs). A conventional LWA is a parallel-plate waveguide with a single open slit on the top plate allowing the guided wave to leak out, albeit at a direction that is correlated with the frequency [3, 18]. We show that with one open slot, LWA can form unique asymmetric spectral characteristics in one angular dimension only; thereby, it cannot enable 3D localization. Instead, we present the first dual-slit THz leaky antenna by incorporating two perpendicular leakage apertures on the top plate of the waveguide. By exciting this architecture with a THz impulse, the underlying frequencies decompose and emit out into free space such that each azimuth-elevation pair adopts a unique spectral fingerprint.

Second, we develop a model that predicts the 3D THz fingerprints based on the physics of EM waves and diffraction principles. Therefore, we enable a receiver to estimate its 3D location by assessing the spectral characteristics (namely, peak

frequency and half-power bandwidth) of the measured signal from a single broadband leaky emission. However, the similarity of angular-spectral patterns emitting from the two slits can cause ambiguity for the RX, who may not be able to distinguish what portion of the received signal originates from each aperture. This could further lead to localization error under practical scenarios with background noise and reflection. To tackle this challenge, we introduce two degrees of freedom in the 123-LOC's architecture; namely, diversity in polarization and leakage geometry. We demonstrate the impact of leakage geometry on the 3D spectral fingerprints and leverage it as a new design space for 3D localization. Further, we propose to exploit orthogonal polarization for the dual-slit emissions. Instead of employing two different sources for the two different polarization channels, we integrate a reflecting splitter into the internal region of the waveguide to generate the two polarization channels from a single source.

Finally, we implement the key components of 123-LOC and perform extensive simulation and over-the-air experiments in various settings. We fabricate a custom dual-slit dual-polarized LWA and deploy it together with a THz impulse generator and a broadband detector. 123-LOC is the first non-coherent training-free 3D localization system in the THz range. Our key contributions are:

- (i) We experimentally characterize the far-field radiations of a single-slit THz waveguide and show that the frequency-dependent directional emission is limited to one angular dimension. In particular, diffraction from a narrow aperture generates a beam whose direction is independent of the frequency in the plane perpendicular to the slit hindering 3D localization.
- (ii) We model and experimentally validate the polarized 3D emissions from a dual-slit waveguide and investigate the dependency of the asymmetric spectral fingerprint on the slit geometry. We emphasize that our model is a deterministic function of the LWA geometric properties and thus can be known a priori by the receiver.
- (iii) Driven by the 3D angular dispersion, an RX with a fixed aperture captures a wider range of frequencies when it is closer to the leaky-wave emitter. We devise an algorithm to infer the TX-RX distance based on the measured half-power bandwidth. Our experimental evaluations show that our non-coherent scheme achieves millimeter-scale ranging accuracy.
- (iv) Similarly, we leverage the unique THz fingerprints to jointly estimate azimuth and elevation angles and enable sub-degree-scale angular localization.
- (v) Even though ambient reflection is expected to be sparse, strong reflection may still occur in certain environments. 123-LOC offers two-layer protection against background reflection. First, by design, signals traveling along the NLOS path have different spectral content which can be used to distinguish the LOS signal from reflection. Second, the polarization vector of incident waves often changes upon reflection, i.e., a linearly-polarized incident signal can create both vertical and horizontal reflected waves, albeit each carrying less power than the original incident signal. Therefore, the RX can identify a reflected path through its weak but identical spectral footprint at the two polarization channels.

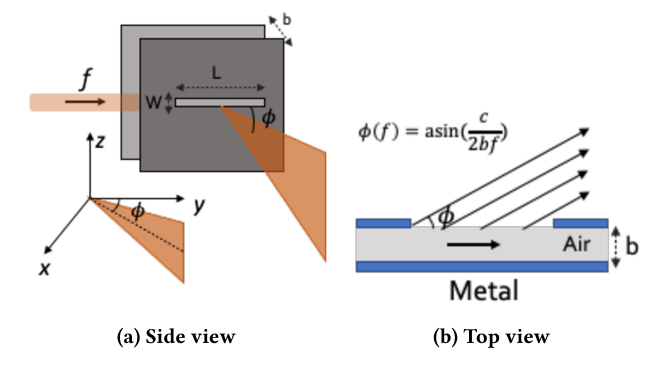


Figure 1: A Leaky Wave Antenna (LWA) in which the input signal emerges from the slot such that the emission angle correlates with the input frequency. The larger the input frequency, the lower the azimuth emission angle in the x-y plane.

The rest of this paper is organized as follows: Sec. 2 provides background on LWAs. Sec. 3 presents the design of 123-LOC. Sec. 4 introduces our experimental platform and Sec. 5 describes the evaluation results. Finally, sec. 6 reviews the related work and Sec. 7 concludes this paper.

#### 2 PRELIMINARY

In this section, we provide background on LWAs and their inherent dispersion characteristics.

#### 2.1 What is a Leaky-Wave Antenna?

A LWA is primarily a metal parallel-plate waveguide with an open slit on one plate. A traveling wave inside the waveguide might "leak" out to free-space if satisfying the boundary conditions on the open aperture [13]. Fig. 1 depicts a LWA device with separation b between the two metal plates. The wave leaks from a single rectangular slit of length L and width W. Interestingly, the direction at which the wave emits out is determined by the waveguide geometry and the frequency of the guided wave. With simplified assumptions on the conductivity and thickness of the metal plate, Maxwell's equations and phase matching conditions yield the following relation for the  $TE_1$  mode [20]:

$$\phi(f) = a\sin\left(\frac{c}{2bf}\right),\tag{1}$$

where  $\phi$  is the azimuth emission angle on the x-y plane (perpendicular to the waveguide plate), f is the frequency of the input signal, c is the free-space light speed, and b is the plate spacing. Eq. (1) indicates that signals with higher frequencies emit out at lower azimuth angles and vice versa.

#### 2.2 One-Dimension Angular Dispersion

The simple monotonic angle-frequency relation of Eq. (1) enables one-dimensional angular sweep by tuning the frequency of the signal injected to the waveguide. This capability has recently enabled ultra-fast path discovery. In particular, [11] proposed to use a single-slit leaky device to simultaneously transmit different frequencies at different azimuthal directions such that the RX is able to extract the angle of departure by assessing the received power spectrum. In the elevation direction (parallel to the metal

plate), diffraction from a sub-wavelength aperture is expected to generate a beam whose direction is independent of frequency; unfortunately, limiting the frequency-dependent angular scanning to the azimuth direction only. Therefore, the inherent quasi-optical diffraction characteristics of this structure hinder 3D localization. This paper presents the first 3D localization scheme using a dual-slit LWA offering azimuth/elevation angle estimation jointly with non-coherent ranging.

# 2.3 Practicality: Fabrication Cost, Coupling Efficiency, and Power Consumption.

LWA structures are composed of two pieces of thin metal being held in parallel with a spacer in between. Thus, the fabrication cost is almost negligible (<\$10). The device is also light weight and passive, suitable for fixed infrastructure (e.g., AP) and mobile users. The coupling efficiency depends on the frequency and waveguide geometry but it is often about 90% [27]. The most power hungry component of this architecture is the broadband signal generator and detector. However, broadband transceivers above 100 GHz have been designed and implemented using CMOS-technology in prior work [4, 33, 35]. With CMOS-technology and production at-scale, the cost of a broadband transceiver in the sub-THz regime would not be significantly higher than existing commercialized transceivers in lower bands.

#### 3 123-LOC DESIGN

In this section, we describe the design of 123-LOC that realizes the first non-coherent 3D localization using asymmetric fingerprints.

### 3.1 Design Overview

Existing wireless localization systems either utilize wideband radios with coherent time-of-flight (ToF) measurements or employ multiple antennas for non-coherent angle-of-arrival (AoA) estimation. The first imposes stringent constraints on the node synchronization while the latter requires large antenna arrays for accurate positioning. This paper targets the best of the two worlds: high accuracy of wideband techniques and simplicity of non-coherent architectures. In particular, we propose 123-LOC, the first non-coherent single-antenna architecture for 3D localization using high-resolution quasi-optical wireless signals at THz frequencies (i.e., above 100 GHz). Indeed, it is the availability of abundant spectrum in this regime that allows for accurate localization based on non-coherent wideband inferences.

123-LOC adopts the inherent dependency of emission angle with frequency in LWAs to correlate spatial information with the spectral properties of the measured signal at the RX. In particular, we inject a short impulse into the waveguide (equivalently, a wideband signal) which will be decomposed into sub-channels each emerging in a different direction at the same time. Unfortunately, a single leakage aperture oriented along  $\overrightarrow{y}$  can only create asymmetric emissions at different azimuth angles in the x-y plane, with a very similar spectral profile across elevation angles. Therefore, the received spectral content fails to convey effective information about the location of an RX in the 3D space.

This paper presents the first dual-slit THz leaky antenna incorporating two perpendicular leakage apertures on the top

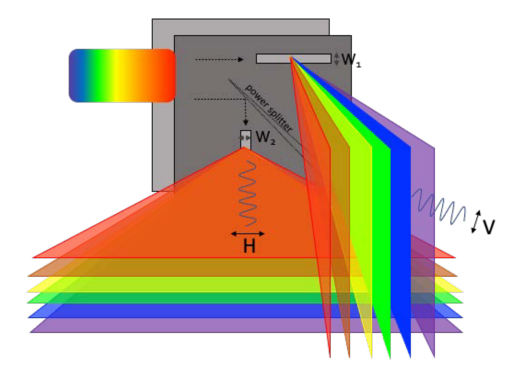


Figure 2: Our dual-slit leaky waveguide structure with an embedded reflecting splitter and two perpendicular open apertures creating 3D frequency-dependent angular dispersion.

plate of a single waveguide. The architecture of 123-LOC is demonstrated in Fig. 2. We excite this waveguide with a broadband signal creating prism-like patterns at both azimuth and elevation angles, as shown in Fig. 2. A portion of these EM waves arrives at the RX (not shown) such that RX's angular location will depend on the spectral characteristics of the received signal. Further, we estimate the distance of the RX to the leaky transmitter by investigating the bandwidth of the received signal. Due to the 3D angular dispersion, a fixed-aperture RX captures a smaller range of frequencies when it is farther from the source of leakage. Hence, this work introduces the first wideband non-coherent wireless ranging system.

The similarity of angular-spectral patterns emitting from the two slits can cause ambiguity for the RX, who may not be able to distinguish what portion of the received signal originates from each aperture. This could further lead to confusion in locating the RX within the overall overlapping broadcast sector. To resolve this ambiguity, we exploit orthogonal polarizations. Instead of using two separate sources, we propose to integrate a reflecting splitter into the internal region of the waveguide intended for splitting the power and rotating the polarization. In particular, this embedded reflecting splitter guides half of the power toward the horizontal slit while the other half is being redirected toward the vertical slit. Through the interaction with the splitter, the polarization vector is rotated by 90 degrees providing 3D angular dispersion of the orthogonally-polarized EM signals. 123-LOC is the first dual-polarized THz leaky architecture.

Our experimental analysis reveals that adopting polarization diversity alone does not entirely solve the ambiguity issue. In practice, randomly polarized leakage from the slits distorts the measurements. Additionally, ambient reflections in the indoor setting may change the polarization of the incident signals. More importantly, when azimuth and elevation are complementary angles, the spectral attributes received from the two slits are identical. To solve this problem, 123-LOC exploits an additional degree of freedom in the leaky-wave device: the leakage geometry. The key idea is that the leaky geometry imposes a deterministic signature on the far-field angler-spectral characteristics. Therefore, the RX is able to distinguish which part of the spectral profile

belongs to each slit, increasing resilience against polarization leakage and background reflection. Next, we illustrate the key design components of 123-LOC.

## 3.2 3D Emission Pattern from a Single-Slit Leaky TX

123-LOC relates the location parameters (range, azimuth angle, elevation angle) to the spectral profile received at the target RX. The first step is to characterize the frequency dependent far-field radiations from a single-slit leaky TX. We consider a parallel plate waveguide excited in the fundamental transverse electric (TE<sub>1</sub>) mode with a rectangular uniform slit of length L and width W as the leakage geometry (see Fig. 1a). Assuming that the electric field is polarized in the z direction and the slot is oriented along the y axis (i.e., the propagation direction of the guided wave is along the y axis), the far-field radiation pattern emitted from a narrow slit can be modeled according to Huygens' principle as the sum of planar (sine) waves with a decaying exponential as follows:

$$G_{AZ}(\phi, f) \propto \int_{-L/2}^{L/2} e^{-j\beta_y y} e^{-\alpha y} e^{jk_0 \cos(\phi) y} dy$$

$$= sinc\Big( (\beta_y - j\alpha - k_0 \cos\phi) \frac{L}{2} \Big), \tag{2}$$

where sinc(x) = sin(x)/x,  $\phi$  is the azimuth angle defined in Fig. 1,  $k_0 = \omega/c$  is the free-space wavenumber,  $\alpha$  is the leakage attenuation, and  $\beta_y$  is the propagation constant. Note that for TE<sub>1</sub> mode and parallel-plate waveguide with an air core, we can write  $\beta_y = \sqrt{k_0^2 - (\pi/b)^2}$ , where b is the plate separation. Eq. (2) shows the dependency of radiation pattern on frequency. The output radiation peaks at the angle at which  $Re\{(\beta_z - j\alpha - k_0 cos \phi) \frac{L}{2}\} = 0$ , which yields to Eq. (1).

We model the emission in the elevation plane again based on the Huygens' diffraction principle. Particularly, we treat the slit as a series of segmented wave sources such that the far-field radiation pattern is made up of contributions from each of these point sources and the relative phases of these contributions. For a slit width of W that is wider than a wavelength, we can find elevation angles  $\theta_{min}$  at which minimum intensity occurs to be  $Wsin(\theta_{min}) = n\lambda$ , where n is an integer other than zero. Infinitely many points (three shown in Fig. 3) produce a continuously varying intensity in the elevation plane, with the first local minima at  $\frac{W}{2}sin(\theta_{min}) = \frac{\lambda}{2}$ . According to Fraunhofer diffraction equation, we can derive the far-field diffraction profile as

$$G_{ELEV}(\theta, f) \propto sinc\left(W\frac{\pi f}{c}sin\theta\right)$$
 (3)

Finally, putting all pieces together, we can derive the 3D radiation of a uniform single-slit parallel-plate waveguide as

$$G(\phi, \theta, f) \propto sinc\left(W\frac{\pi f}{c}sin\theta\right)sinc\left((\beta(f) - j\alpha - k_0cos\phi)\frac{L}{2}\right)$$
 (4)

We will experimentally validate these frequency-dependent emission patterns in Sec. 5.

How does the angular dispersion change with frequency? We have to answer this question for azimuth and elevation angles separately: First, Eq. (2) suggests that the max-intensity azimuthal angle is dictated by the input frequency, i.e., the lower the

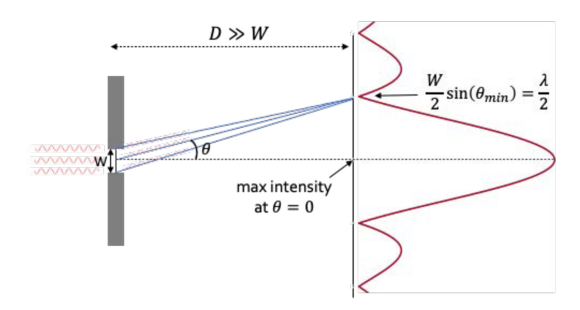


Figure 3: Illustrating Huygens' diffraction principle: Infinitely many points (three shown) along width W project phase contributions from the wavefront, producing a continuously varying intensity across elevation angles.

frequency, the higher the angle of departure. However, that is not the case with the elevation angle. According to Eq. (2), the max-intensity emission angle is always at zero degrees, regardless of the frequency. To demonstrate this statement, we investigate the far-field spectral characteristics at various spatial points in the 3D space. Fig. 4 compares the spectral profile at  $\theta = \phi = 30^{\circ}$ against slightly different azimuth and elevation angles. We observe that the spectral profile is highly sensitive to the azimuth angle as the peak frequency shifts by several GHz per 1 degree of change in the azimuthal direction. This means that the azimuth angles have distinct THz fingerprints that can be used to infer RX's azimuthal angle. The spectral fingerprints at different elevation angles (for a fixed azimuth angle) however are quite similar at least for the stronger frequencies whose normalized amplitude are within the 3 dB of the maximum radiation. For frequencies farther from the peak, we can observe that the elevation angle leaves a clear footprint, i.e., the null frequency is correlated with elevation angle. Yet, the signal strength is substantially weaker (close to the noise level) at those frequencies hindering reliable and accurate localization.

#### 3.3 123-LOC: A Double-Slit LWA Design

Our key idea is to create unique THz spectral fingerprints in 3D so that the received spectral profile at the RX has a one-to-one relationship with the RX's location. Unfortunately, as discussed above, a typical single-slit waveguide cannot provide sufficiently distinct spectral signatures in the 3D space. Hence, we introduce 123-LOC, the first dual-slit THz leaky waveguide that enables joint extraction of azimuth and elevation angles from a one-shot transmission of a THz impulse. In particular, 123-LOC creates unique THz 3D fingerprints by employing the inherent angular-spectral properties of leaky waveguides. The design consists of a parallel plate waveguide with two open slits perpendicular to each other, as also shown in Fig. 2. We embed a reflecting splitter, which is consists of a mirror-like smooth metal surface integrated into the internal region of a parallel-plate waveguide [5]. This passive splitter guides half of the input power toward the horizontal slit and the other half reflects off the splitter and is re-directed toward the vertical slit. We carefully design the position of the power splitter and slits to maximize the out-coupled radiating power.

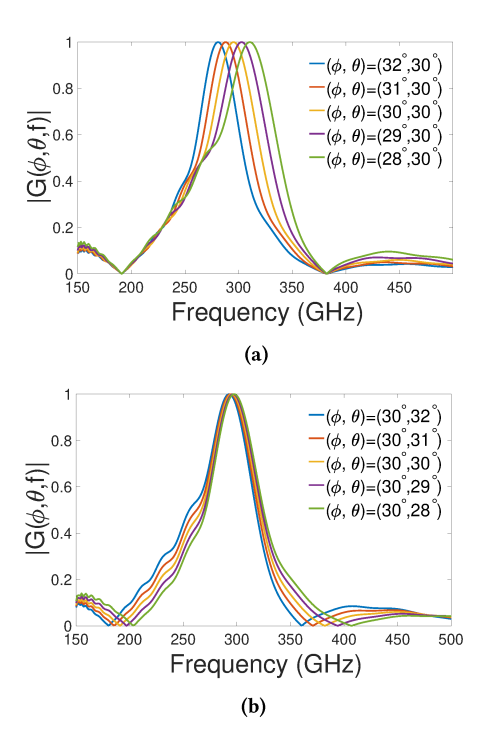


Figure 4: The spectral profile of signals at various 3D spatial points and their sensitivity to changes in the (a) azimuth angles  $(\phi)$  and (b) elevation angles  $(\theta)$ .

An RX at distance d captures the superposition of the radiated signals from the two apertures. When d is much larger than the waveguide dimension, the RX sees the azimuth elevation angle pair of  $(\phi, \theta)$  from the horizontal slit and  $(\frac{\pi}{2} - \theta, \frac{\pi}{2} - \phi)$  from the vertical slit, as depicted in Fig. 5. Our goal is to enable the RX to extract  $\phi$ ,  $\theta$ , and d from the received spectral signatures. Note that such frequency-dependent signatures are a deterministic function of the leakage geometry (width and length) and the waveguide plate separation; thereby, it is fixed upon production and can be known a priori at the RX. Yet, there are two key challenges: (i) the emitted signals from the two apertures may interfere with each other and significantly distort the received spectral content that is used for localization; (ii) the angular-spectral signatures from the two slits are similar except for swapping the azimuth and elevation angle. This similarity causes ambiguity for the RX who may not be able to distinguish azimuth against elevation angles; and (iii) An NLOS path may also carry a portion of the emissions toward the RX's location yielding higher localization errors. Next, we elaborate how 123-LOC tackles the first two challenges and we discuss our NLOS suppression scheme in Sec. 3.4.3.

3.3.1 Resolving Inter-Slit Interference via Polarization Diversity. In 123-LOC, the location information is embedded in the spectral attributes of the receiving signal. Yet, the inter-slit interference may distort, weaken, or even alter these spectral properties that we hope to exploit for localization. To address this challenge, we employ polarization diversity. In particular, we rotate the polarization of emissions from the vertical slit by 90 degrees so that a dual-polarized RX can directly separate the signals received

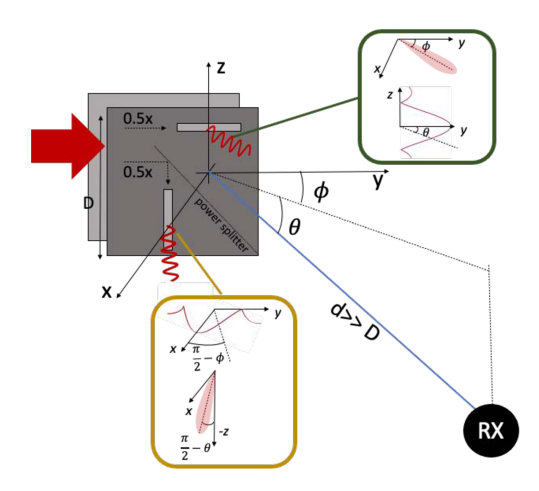


Figure 5: The 3D illustration of the dual-slit waveguide and a far-field RX located at  $(d,\phi,\theta)$ .

from the two perpendicular apertures. A straightforward system implementation would be to employ two different integrated sources, for the two different polarization channels. However, to reduce the hardware complexity and power consumption, it is preferable to use one versatile source, which then requires a rethinking of the antenna configuration in order to generate the two polarization channels from a single source. In particular, by integrating a thin polished piece of metal into the internal region of the waveguide, we can rotate the polarization of reflected waves (which then leak out from the vertical slit) by 90 degrees. Fig. 6 shows the COMSOL simulation of the electric field vector on top of vertical and horizontal slots, showing a 90° shift in the polarization. The magnitude of the vector demonstrates that the radiated power decays along the slit length as most of the input energy out-couples into free space in the first few millimeters of the open aperture (the slit length in this simulation is 30 mm).

A dual-polarized RX can then separate the signal emitted from the two slits as follows

$$R_{1} \propto sinc\left(W\frac{\pi f}{c}sin\theta\right)sinc\left(\left(\beta(f) - j\alpha - k_{0}cos\phi\right)\frac{L}{2}\right),$$

$$R_{2} \propto sinc\left(W\frac{\pi f}{c}cos\phi\right)sinc\left(\left(\beta(f) - j\alpha - k_{0}sin\theta\right)\frac{L}{2}\right),$$
(5)

where  $R_1$  is the vertically-polarized signals captured from horizontal slit (i.e., slit 1 in Fig. 6) and  $R_2$  is similarly the horizontally-polarized

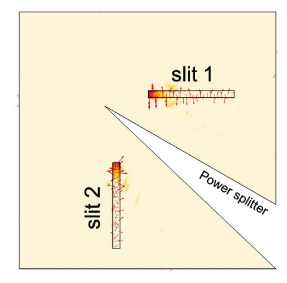


Figure 6: The COMSOL simulation of Electric field vector at both horizontal and vertical slits showing a 90-degree rotation in polarization.

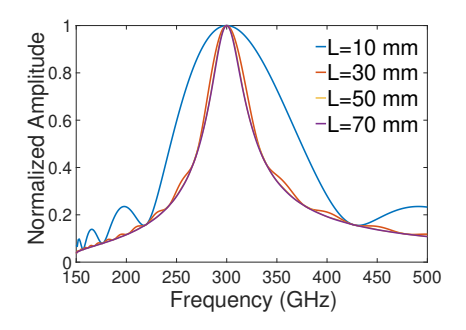
radiations from the vertical slit (i.e., slit 2 in Fig. 6). 123-LOC exploits the measured power spectrums at two polarization channels to localize the RX relative to the dual-slit leaky transmitter.

3.3.2 Resolving Ambiguity via Redesigning the Leakage Geometry. In practice, non-zero cross-polarization at the RX's antenna and polarization rotation due to background reflection prevent the RX to reliably separate the signals originated from the vertical and horizontal slits. Further, an RX with a single polarization channel captures the weighted superposition of polarized emissions from the waveguide depending on its orientation. In such conditions, the polarization alone is not sufficient to distinguish the signals received from the two perpendicular apertures. Finally, even under the LOS channel and zero cross-polarization, the angle estimation can be ambiguous for certain spatial locations. In particular, consider an RX located at  $(d, \phi, \theta)$  such that  $\theta = \frac{\pi}{2} - \phi$ . In this case, the measured angular-spectral patterns from the two slits are identical, according to Eq. (5). Hence, the RX detects one effective leakage aperture and is unable to reliably extract both azimuth and elevation angles.

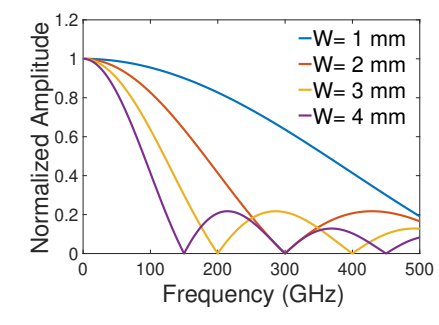
To tackle this ambiguity, our idea is to leverage leakage geometry as a new degree of freedom to manipulate the 3D angular dispersions. In other words, as indicated by Eq. (2) and Eq. (3), the angle-spectral properties of leaky antennas is a function of slit length (L) in the azimuth plane and a function of slit width (W) in the elevation plane. More specifically, the leakage geometry leaves a footprint on the generated THz fingerprints from each slit. Thereby, 123-LOC adopts two distinct leakage geometries for the perpendicular slits so that the RX can differentiate the signals that originated from them. To this end, there are naturally two options: the slits may have different widths or lengths. 123-LOC adopts slit width as a distinguishing factor. To understand the rationale behind this design decision, we will next explain the impact of slit length and slit width on angular-spectral signatures.

**Impact of Slit Length (L).** We first explore the impact of slit length on the spectral signatures in Fig. 7a. We consider an aperture with a fixed width of 2 mm and vary the slit length from 10 to 70 mm. We can observe that, except for L=10 mm, the power spectrum variation is negligible with varying slit length. In the special case of L=10 mm (or generally when L < 10W), the slit is not long enough for complete emission of guided waves and hence our previous models do not hold true anymore. We conclude that employing different slit lengths for the two leakage apertures does not create distinct spectral signatures.

Impact of Slit Width (W). Fig. 7b shows the normalized amplitude vs. frequency for various values of slit width. As shown, the slit width affects the bandwidth radiated at any particular angle. Note that in this plot, the elevation angle is fixed to 30 degrees but a similar trend follows at any other angles. In particular, a narrower slit creates a broader spectral pattern at each direction while increasing W shifts the local minimum to lower frequencies (e.g., 300 GHz for W=2 mm and 200 GHz for W=3 mm). Note that we use a plate spacing of 1 mm which imposes a cutoff frequency of  $\sim 150$  GHz for the TE $_1$  mode meaning frequencies below 150 GHz cannot leak out from the slits. Hence, our spectral range of interest is 150-300 GHz. In 123-LOC, we choose slit the width of 4 mm for the horizontal slit and 1 mm for the vertical slit as they provide sufficiently distinct spectral patterns. Finally, we highlight that the



(a) Impact of Slit Length



(b) Impact of Slit Width

Figure 7: Leakage geometry as a new degree of freedom for manipulating angular-spectral fingerprints.

slit width should be in the order of the wavelength; otherwise, the explained angle-frequency relationship would not hold true [15].

#### 3.4 Non-Coherent 3D Localization

In this section, we explain our non-coherent single-shot localization scheme. Non-coherence refers to the use of power (albeit across a range of frequencies) and not phase or timing information. This methodology, which is motivated by the quasi-optical behavior of THz waves, has several inherent advantages over the phase or ToA-based techniques. In particular, while THz-scale phase information might seem the perfect opportunity to obtain millimeter-scale location information, the sensitivity to synchronization poses a threat in real-world systems that can easily lose track of  $2\pi$  changes, if phase is not tracked continuously at THz timescales. Thus, phase errors between transmissions would be hopelessly error-prone for localization. Instead, our non-coherent framework eliminates the need to keep a tight synchronization and simplifies the node architecture. Further, 123-LOC requires one single transmission of a THz impulse from our dual-slit leaky antenna; thereby, the location can be estimated in nanosecond timescales for real-time location tracking.

3.4.1 Azimuth and Elevation Angle Estimation. 123-LOC exploits the 3D angular dispersions to infer azimuth and elevation angles. We input a broadband THz impulse into our dual-slit waveguide and model the 3D angular dispersion as a function of frequency according to Eq. (5). We then employ a dual-polarized RX to measure the intensity across a range of frequencies with a fixed resolution determined by the RX's clock rate. In our testbed, the RX sampling rate provides an inter-sample spacing of 4 GHz. Azimuth and

ó

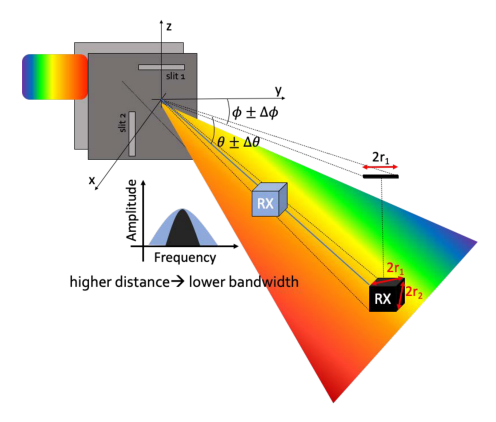


Figure 8: Illustration of our non-coherent ranging scheme mapping signal bandwidth to distance.

elevation angles can be estimated by comparing the measured dual-polarized signal against our model in Eq. (5). Specifically, we form the following optimization framework to minimize the Euclidean distance between measurement data points and our model:

$$\begin{aligned} \{\phi^{\star}, \theta^{\star}\} &= \underset{\theta, \phi}{\arg \min} ||R_{1}(W_{1}, f_{1}: f_{N}, \phi, \theta) - \mathbf{R}_{v}^{ms}||^{2} \\ &+ ||R_{2}(W_{2}, f_{1}: f_{N}, \phi, \theta) - \mathbf{R}_{h}^{ms}||^{2}, \end{aligned} \tag{6}$$

where  $W_1=4$  mm and  $W_2=1$  mm are the width of the horizontal and vertical slits, respectively.  $R_v^{ms}$  denotes the vector of measurement at vertical polarization across the spectral range of interest (i.e.,  $f_1=150$  GHz to  $f_N=300$  GHz) corresponding to the horizontal slit (i.e., slit 1). Similarly,  $R_h^{ms}$  is the measured horizontally-polarized signal from slit 2. We apply appropriate normalization factors to ensure comparability between data and our model. Indeed, the spectral profile (i.e., power distribution across the spectrum) conveys location information and not the absolute power values.

To solve this optimization problem, we initialize  $\phi_0 = asin(\frac{c}{2bf_{ph}})$  and  $\theta_0 = \frac{\pi}{2} - asin(\frac{c}{2bf_{pv}})$  where  $f_{ph}$  and  $f_{pv}$  represent the measured peak frequency that were originated from horizontal and vertical slits, respectively.

3.4.2 Non-coherent Ranging. Thus far, we have illustrated the 3D angular estimation using the spectral fingerprints created by our dual-slit leaky waveguide architecture. The last missing piece is inferring the TX-RX distance. We exploit spectral attributes of the received signal and enable non-coherent millimeter-scale range estimation for the first time. As the space is filled with asymmetric spectral signatures, a RX would capture a wider set of frequencies if located closer to the leaky transmitter and a narrower spectral band farther from the RX. The bandwidth of the received signal is therefore correlated with the TX-RX distance, as also illustrated in Fig. 8. We emphasize that the leakage geometry (i.e., slit width) and the RX aperture size also play an important role in the spectral width. However, such parameters are fixed upon production and can be known in advance.

Without loss of generality, consider an RX at  $(d, \phi, \theta)$  whose aperture is a rectangular cuboid with face diagonals  $2r_1$  and  $2r_2$ , as shown in Fig. 8. Hence, the effective acceptance azimuth angles

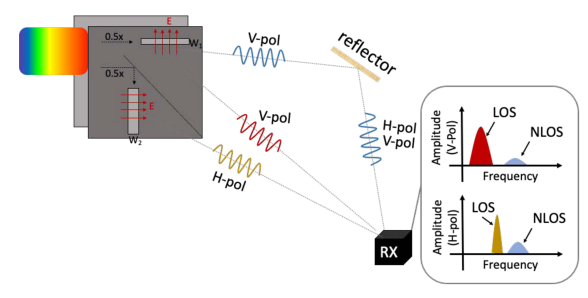


Figure 9: NLOS mitigation in 123-LOC through angle-frequency coupling, polarization switching, and aperture diversity.

can be approximated as  $\phi \pm \Delta \phi$ , where  $\Delta \phi = atan(\frac{r_i}{t})$ . For a given acceptance angle,  $\Delta \phi$ , of a receiver located in the far-field of the slot, the spectral bandwidth of a given channel is described by [20]

$$BW(\phi) = \left| \frac{df}{d\phi} \right| \times 2\Delta\phi = \frac{c}{bsin\phi tan\phi} \Delta\phi, \tag{7}$$

where  $BW(\phi)$  denotes the spectral band as a function of azimuth angle. We can similarly define the effective acceptance elevation angle as  $\theta \pm \Delta \theta$ . Therefore, leveraging the frequency-dependent angular dispersions in the azimuth plane (created by slit 1) or in the elevation plane (created by slit 2) can give us

$$d^{\star} = r_1 \times \cot\left(BW(\mathbf{R}_v^{ms}) \times \frac{c}{b} \sin\phi^{\star} tan\phi^{\star}\right) \text{or}$$

$$d^{\star} = r_2 \times \cot\left(BW(\mathbf{R}_h^{ms}) \times \frac{c}{b} \sin\theta^{\star} tan\theta^{\star}\right), \tag{8}$$

where BW(.) denote the measured spectral bandwidth,  $\phi^*$  and  $\theta^*$  are the estimated azimuth and elevation angles from Eq. (6), and  $d^*$  is the estimated TX-RX distance. Note that in principle the emissions from a single slit are sufficient for such non-coherent ranging. We use maximum ratio combining to combine the h-polarized and v-polarized measurements. We emphasize that our ranging scheme solely relies on the bandwidth of the power spectrum and does not use any phase or timing information.

3.4.3 Suppressing NLOS Interference with Polarization and Aperture Diversity. The presence of ambient reflection poses a challenge for all wireless localization systems since NLOS paths introduce distortions in the phase, time, or power measurements [16, 44, 46]. Even though mmWave and sub-THz channels tend to be sparse, prior work shows the possibility of strong reflection [8]. It is therefore critical to identify and suppress NLOS interference. 123-LOC offers a two-layer protection against background reflection:

First, due to angular dispersion, signals traveling along the NLOS path have different spectral content. Fig. 9 demonstrates an example scenario where the NLOS path carries an EM wave (in blue) while a red-color wave (lower frequencies) travels along the LOS path. Hence, by design, the NLOS path can be distinguished from the LOS path through their spectral profile [11]. Second, the reflective objects may rotate the polarization of the incidental signals upon reflection. Specifically, a linearly-polarized incident signal can induce both vertically and horizontally polarized reflections with the summation of reflected power being smaller

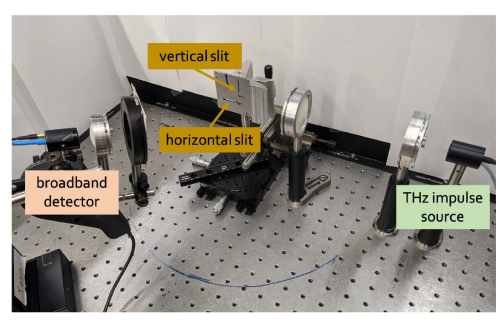


Figure 10: Our experimental setup.

than the incident power. Therefore, the RX can identify a reflected path through its weak but identical spectral footprint at the two polarization channels, as depicted in Fig. 9. Further, we can identify whether or not the LOS and NLOS paths are originated from the same slit by investigating the spectral footprint of leakage geometry. For instance, in Fig. 9, the LOS signal from the vertical slit has narrower bandwidth, due to a larger slit width, compared to signals (LOS and NLOS) emitting from the horizontal slit.

# 4 EXPERIMENTAL PLATFORM AND METHODOLOGY

We conduct extensive COMSOL simulations and over-the-air experiments to characterize our dual-slit waveguide structure and evaluate the performance of 123-LOC. We build a custom waveguide with thin metal plates and plate separation of 1 mm (i.e., b=1 mm). We cut a horizontal slit of 3 cm long and 4 mm wide and a vertical slit of 3 cm long and 1 mm wide. Between the metal plates, we embed a reflecting splitter which consists of an ideal mirror-like smooth metal surface. In this proof-of-concept system, the waveguide geometry is not optimized for the minimum size. The length of the aperture should be an order of magnitude larger than the plate separation (i.e., 1 cm) to allow the guided wave to efficiently leak out from the waveguide. Also, one can optimize the placement of the slits and the leakage shape to maximize the out-coupled power at any given waveguide dimension.

For broadband transmission and detection, we use the TOPTICA THz time-domain spectroscopy (TDS) system. This system uses a laser is to generate a 1560 nm femtosecond pulse and illuminate InGaAs photoconductive antennas (PCA) at the emitter and detector. The fiber-coupled emitter generates the THz signal and the detector measures a photocurrent proportional to the electric field of the THz pulse. The emitter and detectors have an integrated Si lens and are both linearly polarized.

Fig. 10 shows our measurement setup. The THz pulse is focused into the waveguide antenna via two 6 cm Teflon lenses 12 cm apart. An additional taper is attached to the input of the waveguide in order to improve input coupling. The receiver is mounted on a 2D linear translational stage (not shown) and can be configured in various azimuth and elevation directions. A 3 cm Teflon lens is mounted onto the receiver and a hot-stamped polarizer is placed in front of the lens eliminating cross polarizations [14]. Our RX can record one polarization channel at a time. Both the polarizer and the receiver were adjusted appropriately when targeting a specific polarization.

Our broadband source is bulky and extremely low-power with an average output power of roughly -10 dBm integrated over 1 THz of the spectrum. Thereby, due to this limitation, we are bound to conduct top-table experiments with ranges up to 1 meter. However, this limitation is solely due to the lack of sufficient output power and not the architecture of our dual-slit waveguide. Increasing the power emitted by the TX can scale up the transmitter-receiver distance as links at WLAN-scale distances (100+) meters have already been demonstrated at many frequencies above 100 GHz [42, 43]. Although the deployment of this broadband source is impractical in future mobile devices, our setup is meant to investigate the ability of the proposed asymmetric signatures above 100 GHz in accurate 3D localization. State-of-the-art CMOS-based solutions for wideband tunable sources achieve about -10 dBm of power in 1 KHz of bandwidth [4], offering a nine order of magnitude increase in output spectral intensity compared to our THz system. Therefore, when integrated with our dual-slit node, it can enable 3D localization at much larger ranges. The leaky waveguide itself can be realized via an integrated circuit. Indeed, recent work such as [34] has developed a Leaky Wave Antenna based transceiver in 65nm CMOS with an area size of  $3mm^2$ . Such implementations are inherently more scalable, low-cost, and lightweight for future mobile applications.

#### 5 EVALUATION

In this section, we discuss our over-the-air experiments and evaluate the key design components of 123-LOC.

# 5.1 Characterization of 3D Emissions in Single-Slit Waveguides

We first experimentally characterize the 3D emission pattern of a single-slit leaky-wave antenna and validate the idealized model proposed in Sec. 3.2.

**Setup.** We deploy our THz time-domain system for pulse generation and fabricate a leaky-wave device with a single 1 mm-wide aperture. We configure the RX at different azimuth and elevation angles covering a range of  $10^{\circ} - 80^{\circ}$  for azimuth angles and  $0^{\circ} - 60^{\circ}$  in the elevation direction. We collect raw time-domain samples and apply conventional signal processing techniques (smoothing, filtering, FFT, etc.). Note that even though our testbed provides time-domain signals, 123-LOC only relies on power spectrum for estimation and not phase or timing information.

Fig. 11 shows the measured far-field emissions across azimuth and elevation angles for a few frequencies, namely, f=200,210,220,230 GHz. In Fig. 11a, the RX is configured at multiple azimuth angles in the x-y plane ( $\theta=0$ ). We observe a clear frequency shift as predicted by the model in Eq. (2). For angles far from the peak, irregularities can be seen in the measured power spectrum that is not captured by our idealized model that assumes the metal in which the slot has been cut is infinitely thin and infinitely conductive. However, such irregularities have second-order effects as their signal strength is substantially weaker.

Further, Fig. 11b depicts the distribution of power vs. elevation angles for the same set of frequencies. In this setting, the azimuth angle is set to 45 degrees. As predicted by our idealized model (Eq. (3)), the emitted power is maximum at the x-y plane and

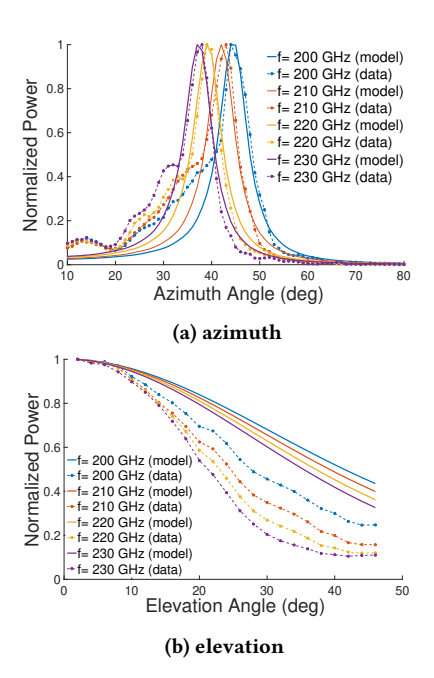


Figure 11: Experimental evaluation of the 3D emission characteristics of a single-slit leaky waveguide.

gradually decays at higher elevation angles. Also, we observe that the fall-off rate increases slightly at higher frequencies. Even though our model correctly predicts the angular and spectral trends, it consistently underestimates this fall-off rate. This is because the actual value would depend on the wavefront beneath the slot and those details are not taken into account here and do not impact the localization performance.

We have experimentally demonstrated that diffraction from a narrow aperture generates a beam whose direction is independent of the frequency in the plane perpendicular to the slit. Therefore, angular positioning with a conventional single-slit LWA is limited to one dimension only.

# 5.2 Polarized 3D Spectral Signatures via Dual-Slit Leaky Structure

Next, we deploy the dual-slit leaky structure and experimentally characterize the angular-spectral patterns in both polarization channels. We use the same setup as in Fig. 10 and place the RX at various configurations. First, we set the elevation angle to 20 degrees and vary the azimuth angle. Fig. 12a depicts the measured power spectrum with a vertically polarized receive antenna. Recall that waves emitting from the horizontal slit have vertical polarization and emission from the vertical slit is horizontally polarized. Hence, the vertical channel should ideally measure the signals originated from the horizontal slit whose spectral attributes should change with azimuth angle. Fig. 12a confirms a shift in peak frequency consistent with the model, namely,  $R_2$  in Eq. (5). Nonetheless, the signal polarization is not perfect leading to cross-polarization leakage. Fig. 12a shows the impact of such interference specifically at  $\phi = 70^{\circ}$  causing irregularities in the spectral profile. Generally, when the interfering slit is oriented

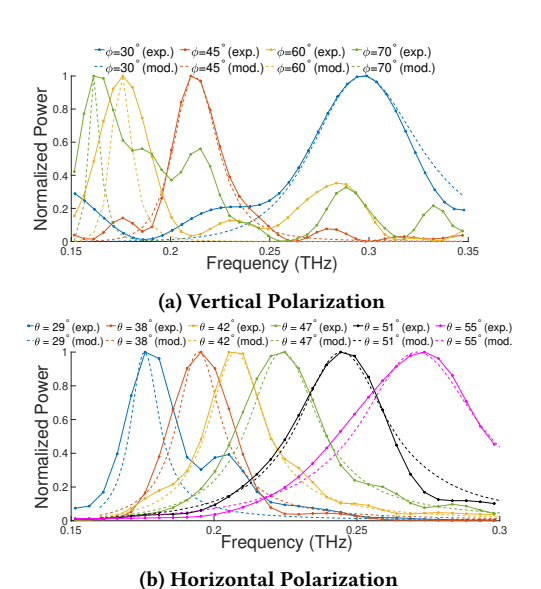


Figure 12: The experimental characterization of polarized 3D spectral signatures.

along the z-direction (as shown in Fig. 5), the interference is higher when the RX is located on the y-z plane (i.e., around  $\phi = 90^{\circ}$ ).

Similarly, Fig. 12b demonstrates the measured power spectrum via a horizontally polarized RX at various elevation angles and fixed  $\phi=70^\circ$ . Unlike emissions from a single-slit that manifest almost identical spectral profiles at various elevation angles, Fig. 12b reveals a clear shift in peak frequency as a function of  $\theta$ . Moreover, the measured angular-spectral signatures are in agreement with the developed model in Sec. 3; namely,  $R_2$  in Eq. (5). The imperfect polarization switching again yields an inter-slit interference causing second-order irregularities at  $\theta=29^\circ$  where the interference from the horizontal slot is stronger. Nonetheless, the peak frequency and the overall spectral profile closely follow the model.

We have experimentally validated our proposed model that characterizes the THz fingerprints as a function of azimuth and elevation angles. While our model does not capture the second-order irregularities due to the cross-polarization leakage, it can accurately predict the angle-frequency correlations, which 123-LOC leverages for 3D localization.

# 5.3 Impact of Aperture Size on Spectral Signatures

123-LOC uses leakage geometry to manipulate the frequency-dependent emission from the waveguide. Specifically, different slit widths are adopted for the vertical and horizontal slits so that the RX can distinguish the spectral patterns that originated from the two slits. Fig. 13 shows the power distribution across elevation angles when a single-slit waveguide with a slit width of 1 mm, 3 mm, or 4 mm is deployed. This plot shows the result for  $f=200~{\rm GHz}$  but similar a trend follows at other frequencies. The COMSOL simulation results are inconsistent with our model in Eq. (3) showing that the diffraction from a narrow aperture generates a beam toward  $\theta=0$ , independent of the slit width. However, slit width has a significant impact on the power reduction rate at higher elevation angles, i.e.,

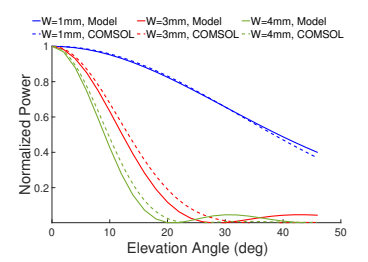


Figure 13: Impact of Aperture Width on the Directional Emission from a Single-Slit LWA.

the beamwidth of the transmission. Hence, the slit width does not impact the direction of emission but can manipulate the power distribution over the spectral band of interest.

We have shown that by widening the aperture of one slit, we can manipulate the emissions from the LWA to have slightly different angular-spectral signatures.

## 5.4 3D Localization Accuracy

Next, we assess the localization accuracy of our non-coherent angular positioning and range estimation.

5.4.1 Angular Location Estimation. We deploy a dual-slit LWA and place the RX as multiple  $(\phi,\theta)$  configurations. We then input a THz impulse into the waveguide and measure the power spectrum at two orthogonal polarization channels. For comparison purposes, we take two approaches for angle estimation. In particular, we run our optimization framework explained in Eq. (6) using spectral samples in the vicinity of the peak frequency (within 1 dB) and once again with the entire power spectrum in the range of 150 – 300 GHz.

Fig. 14a and Fig. 14b present the estimation results in azimuth and elevation directions, respectively. For each azimuth (elevation) angle, we place the RX at multiple elevation (azimuth) configurations and the plots show the corresponding average and standard deviations. 123-LOC achieves an average estimation error of < 1° using the high-intensity measured spectral components close to the peak frequency. The estimation error is slightly higher (< 3°) when the entire power spectrum is used. We observe a higher error when  $\phi > 55^{\circ}$ . The reason is two-fold: (i) the spectral fingerprints are similar (but not identical) at higher  $\phi$ (see Eq. (1)) making them vulnerable to estimation errors; and (ii) the cross-polarized leakage from the vertical slit is stronger at those angles. Similarly, Fig. 14b shows a higher estimation error at  $\theta < 40^{\circ}$  due to the non-negligible cross-polarized leakage from the horizontal slit. Such leakages would cause irregularities in the measured power spectrum (discussed also in Fig. (12b)) that are not captured by our idealized model. Nonetheless, the cross-polarized leakage is weak relative to the peak frequency, which is reflected in the better localization performance.

5.4.2 Range Estimation. The angular dispersion in leaky-wave emission allows for non-coherent one-shot TX-RX range estimation. In particular, since the effective acceptance angle of the RX decreases with distance, we expect smaller bandwidth at longer ranges and vice versa. Hence, 123-LOC translates the measured half-power bandwidth to the RX's distance from the leaky-wave

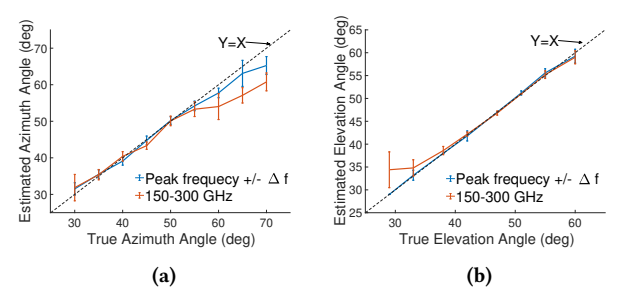


Figure 14: Performance evaluation of the angular location estimation in 123-LOC: (a) azimuth direction; (b) elevation direction.

antenna. To verify our ranging design principle, we first fix the RX's angular positions ( $\phi=45$  and  $\theta=0$ ) and vary its distance. As shown in Fig. 15, the half-power bandwidth is narrowed down on both sides (high-frequency and low-frequency components) at farther distances.

Next, Fig. 16a presents the measured bandwidth vs. distance and compare it against our model, i.e., Eq. (7). In order to be able to directly compare the modeled bandwidth with measured bandwidth, we need to calculate a calibration factor which is a fixed scalar that depends solely on the RX aperture size and shape. This calibration factor is calculated by measuring the spectral signatures and specifically the received 3dB bandwidth at several distances and angular configurations. We then fit the measured bandwidth and the ground truth locations to the model in Eq. (7) and find the effective acceptance angle, i.e.,  $\Delta \phi$ . Note that  $\Delta \phi$  may not necessarily relate to the physical dimension of the RX. We keep the effective aperture fixed for our test data points. <sup>1</sup> Since the RX aperture is fixed upon production, this calibration factor can be hardcoded to the RX and be known a priori. According to Fig. 16a, our experimental measurements consistently follow the model.

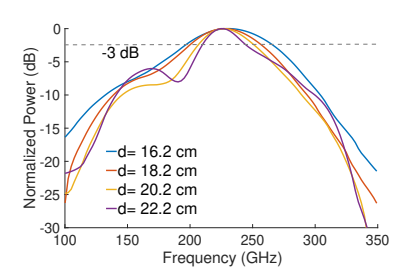


Figure 15: The received power spectrum at various distances from a leaky-wave transmitter.

Finally, Fig. 16b shows the empirical distribution function of the estimation error. The ranging estimation error is 4.4 mm on average and is less than 10 mm throughout the experiments. We emphasize that such mm-scale ranging accuracy is achieved through non-coherent measurement of a one-time transmission of a THz impulse via a leaky-wave structure. By design, the performance of our localization scheme highly depends on the

 $<sup>^1 {\</sup>rm In}$  our experiments, for an RX with a circle-shaped aperture of radius 2 cm, the calibration factor is  $60/\pi.$ 

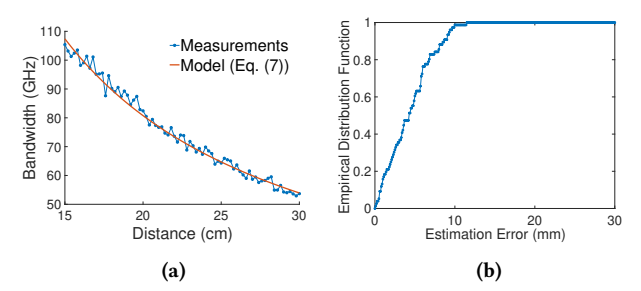


Figure 16: Performance evaluation of non-coherent range estimation in 123-LOC: (a) BW reduction as a function of distance; (b) estimation error.

spectral resolution, i.e., the clock sampling rate. Our results reveal that even with a 4-GHz frequency resolution, the estimation error is at millimeter scales. According to Eq. (7), the BW is proportional to  $atan(\frac{r_1}{d})$ . In the far-field, we always have  $r_1 \ll d$  and hence the  $BW \propto \frac{1}{d}$ . Therefore, we expect that better spectral resolution is needed to maintain the mm-scale localization accuracy at larger distances. Unfortunately, due to hardware limitations (namely, ultra-low transmission power), our experiments are conducted at sub-meter distances.

We have experimentally demonstrated that 123-LOC achieves millimeter-scale ranging resolution jointly with sub-degree estimation accuracy in angular positioning through non-coherent measurements.

#### 5.5 Evaluating Power and Range Performance

So far all experiments have been conducted in the short range of up to 30 cm. Here, we demonstrate that increasing the distance would not alter the inherent spectral characteristics of received signal; thereby, the limitation on the achievable range is solely a function of the limited transmit power in our setup. To this end, we increase the distance between the leaky-wave device and the RX from 20 to 76 cm and record the signal. The angular location of the RX is set  $\phi=45$  and  $\theta=0$ , corresponding to an expected peak frequency of 211 GHz based on Eq. (1) when b=1.0 mm. Fig. 17a shows the peak frequency of the captured signals. As expected, the peak frequency remains constant with changing distance.

Next, we break down the link budget in our setup. We first measure the source output power by placing the RX as close to the source as physically possible and observe a total  $|V|^2 = 3.4241 V^2$ in the range of 150 to 300 GHz<sup>2</sup>. Then we put the RX at the exact location of our leaky device (see Fig. 10). The measured power at this position represents the total input power to the waveguide and we refer to it as the reference power. Fig. 17b shows the total received power relative to this reference power (i.e., the injected power being 0 dB). We also show the measured noise level for the same RX placement. The noise level is measured at the same frequency band and by blocking the TX. For comparison purposes, Fig. 17b also demonstrates the Friis path loss model at 211 GHz (the peak frequency). We observe that at distances below 50 cm, our total measured power (in the 150-300 GHz band) is larger than expected. This initial deviation is attributed to the signal's large but decaying bandwidth that is ignored in the single-tone Friis model. However, as the TX-RX distance increases the bandwidth shrinks

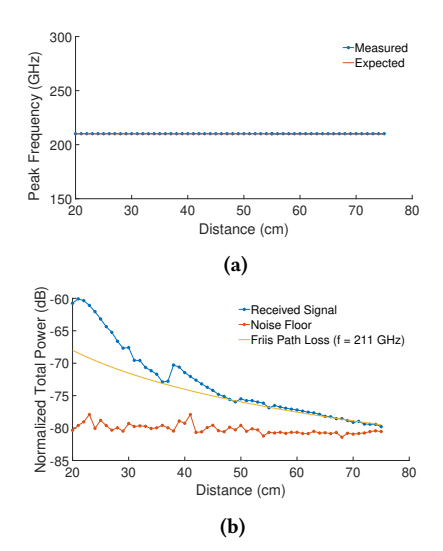


Figure 17: Experimental Range Performance: (a) Peak Frequency; (b) Normalized Power Loss.

and the signal level naturally gets closer to the noise level, as also characterized by Friis path loss for the peak frequency. We leave the investigation of larger TX-RX distances for future work.

We have demonstrated that the inherent spatial-spectral properties of our design are independent of communication range. Due to our hardware limitations (ultra-low power source) and the significant path loss above 100 GHz, the signal level rapidly approaches noise level for longer distances beyond 70 cm in our measurements. Yet, 123-LOC can be naturally extended to larger distances using other wideband sources from the literature.

#### 5.6 Evaluating NLOS Mitigation

Lastly, we investigate the key components of 123-LOC for NLOS mitigation. To this end, we deploy the setup depicted in Fig. 9 and place a reflector at 45° relative to the horizontal slit. The RX itself is located at  $\phi=60^\circ$  and measures the signal at both polarization channels. As shown in Fig. 9, the H-polarized antenna should capture the LOS emission from the vertical slit as well as any potential reflection. To isolate the spectral profile of the NLOS path, we manually block the vertical slit for this experiment only and plot the measured power spectrum in Fig. 18.

We can observe the NLOS footprint at both polarization channels in the form of local peaks at the same frequency in the measured power spectrum. This result indicates that the reflector rotates the polarization vector of the incident waves from linear to circular. Indeed, this polarization rotation is prevalent for ambient reflection as an object rarely induces reflection whose polarization vector is perfectly parallel or orthogonal to that of the incident waves. Moreover, since the reflector and the RX are positioned at different angles, the signal that bounces off the reflector has distinct spectral content by design (angular dispersion and aperture diversity); thereby, can be separated from the signals that directly reach the RX. In Fig. 18, the LOS signal contains frequencies around 173 GHz seen only at the vertical channel.

NLOS mitigation in the presence of multiple reflections is not straightforward as it yields to the superposition of multiple

 $<sup>^2 \</sup>mathrm{Since}$  the internal impedance is not given, we cannot directly convert  $|V|^2$  to Watts.

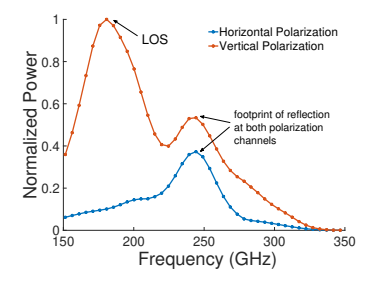


Figure 18: Experimental demonstrating of the NLOS mitigation principle in 123-LOC.

dual-polarized waves with different spectral profiles that might partially overlap in time and/or frequency. In the case of multiple first-order reflections, we can identify the NLOS paths from their almost-identical spectral pattern in both polarization channels as opposed to the LOS spectral footprint that can only be seen in one polarization channel. However, in a rich scattering environment (that is uncommon above 100 GHz), there is an increasing chance of NLOS interference that may lead to ambiguity in LOS identification and localization. Given that the spectral content of each NLOS path is unique to its angle of departure, such interference is more likely to occur when the spectral fingerprints of multiple paths overlap in the frequency domain, i.e., when their angles of departure are not sufficiently apart. We will leave the investigation of multiple NLOS paths and their impact on the localization accuracy for future work. Higher-order reflections pose less of an issue as they are much weaker relative to the LOS signal due to the longer path length and reflection attenuation. As explored in [30, 31], second-order reflections are not common above 100 GHz given the additional tens of dB of attenuation.

Our localization system identifies the distortion caused by ambient reflection via its district spectral footprint that is captured at both polarization channels.

#### 6 RELATED WORK

In this section, we first review existing 3D localization technologies and then discuss the history of LWAs.

Wireless Localization and Tracking. Accurate localization systems have various applications in elder and patients monitoring [28], motion tracking [32, 40], gesture sensing and tracking [36, 38], and even smart surgery [39]. Recent 3D localization systems are implemented with diverse wireless technologies. Conventional systems adopt ToA or TDoA measurements using UWB radios [21, 22, 47] or FMCW technology [1, 48], which can provide accurate location estimations. While these methods achieve good accuracy, they require a coherent RX design to extract timing information. In contrast, we introduce a *non-coherent* 3D localization scheme with a single wideband antenna that does not require phase or ToA measurements.

Another body of work focuses on leveraging ubiquitous WiFi infrastructure for localization [49]. Specifically, various AoA estimation techniques were proposed to achieve sub-meter localization using Wi-Fi devices. Since the AoA resolution relies on the number of antennas in multipath indoor environments, such localization systems require many antennas in the node

architecture to achieve high accuracy [17, 19]. Thereby, to enhance AoA accuracy with a limited number of available antennas on the COTS WiFi devices, the state-of-the-art realizes joint AoA and ToA estimations [12, 41]. Instead, 123-LOC utilizes a dual-slit leaky antenna in the TX and RX physical layer and provides AoA estimation in both azimuth and elevation planes with sub-degree accuracy.

Finally, significant advances have been made in machine-learning assisted localization. Current solutions essentially adopt one of the aforementioned techniques (i.e., exploiting ToA measurements with a UWB/FMCW radio or estimating AoA using multiple antennas) and integrate them with data-driven strategies to enhance localization accuracy by NLOS mitigation, parameter optimization, and developing distributed cooperative algorithms [2, 36, 37, 48]. Such efforts are complementary to our solution and 123-LOC can also benefit from leveraging machine learning models to boost performance, particularly at longer distances.

Leaky Wave Antennas. Early demonstrations of LWAs in the microwave regime go back to a few decades ago [3, 18]. Parallel-plate waveguide antennas have shown to be promising for THz beam steering, due to their low-loss and low-dispersion characteristics [7, 23-27, 34, 45]. More recently, single-shot path discovery and one-dimensional angular motion tracking have been proposed by exploiting a single-slit leaky-wave antenna [9-11]. Nevertheless, these works are limited to 2D path discovery. As evident from our results in Eq. (1) and Eq. (3), extracting the elevation angle for 3D localization is not possible with a single-slit waveguide that creates a fan-shaped beam for a given input frequency. This paper introduces the first dual-slit THz leaky-wave antenna that is able to able to efficiently perform 3D localization. Using a single anchor, we show how to jointly estimate range, elevation, and azimuth angles via one-shot non-coherent measurements. Finally, we exploit leakage geometry together with polarization diversity to increase resilience against background reflections and non-idealities of the antenna.

#### 7 CONCLUSION

In this paper, we present 123-LOC, a novel structure that enables non-coherent 3D localization in the THz range. 123-LOC adopts the inherent dependency of emission angle with frequency in leaky-wave antennas to create distinct 3D angular-spectral fingerprints for joint estimation of azimuth angle, elevation angle, and TX-RX distance. The proposed architecture incorporates a metal parallel-plate waveguide in which two perpendicular thin slits are cut on the top plate. We create 3D angular dispersion by injecting a THz impulse and enabling simultaneous emissions from both slits. To distinguish the spectral patterns originated from each slit and mitigate NLOS reflection, 123-LOC exploits diversity in polarization and leakage geometry. Our over-the-air experiments show that 123-LOC achieves angular positing estimates within 1° of ground truth jointly with millimeter-scale ranging accuracy.

### 8 ACKNOWLEDGMENTS

We appreciate the valuable comments and feedback from the anonymous reviewers. This research was supported by Army Research Laboratory, Cisco, Intel, and NSF grants CNS-1955075 and CNS-1923782.

#### REFERENCES

- Fadel Adib, Zach Kabelac, Dina Katabi, and Robert C Miller. 2014. 3D Tracking via Body Radio Reflections. In Proc. USENIX NSDI.
- [2] Roshan Ayyalasomayajula, Aditya Arun, Chenfeng Wu, Sanatan Sharma, Abhishek Rajkumar Sethi, Deepak Vasisht, and Dinesh Bharadia. 2020. Deep Learning Based Wireless Localization for Indoor Navigation. In Proc. of ACM MobiCom. Article 17, 14 pages.
- [3] Constantine A Balanis and Craig R Birtcher. 2008. Antenna Measurements. Modern Antenna Handbook (2008), 977–1033.
- [4] Taiyun Chi, Min-Yu Huang, Sensen Li, and Hua Wang. 2017. 17.7 A Packaged 90-to-300GHz Transmitter and 115-to-325GHz Coherent Receiver in CMOS for Full-Band Continuous-wave mm-Wave Hyperspectral Imaging. In Proc. of IEEE ISSCC.
- [5] S Coleman and D Grischkowsky. 2003. A THz Transverse Electromagnetic Mode Two-Dimensional Interconnect Layer Incorporating Quasi-Optics. Applied physics letters 83, 18 (2003), 3656–3658.
- [6] Federal Communications Commission. Mar. 2019. James Edwin Whedbee Petition for Rulemaking to Allow Unlicensed Operation in the 95-1,000 GHz Band. ET Docket 26, 18-21 (Mar. 2019).
- [7] María García-Vigueras, Marc Esquius-Morote, and Juan R Mosig. 2015. Dual-Polarized Directional Antenna with Application to Polarimetric Radar. In IEEE International Symposium on Antennas and Propagation & USNC/URSI National Radio Science Meeting. IEEE, 27–28.
- [8] Yasaman Ghasempour, Yasith Amarasinghe, Chia-Yi Yeh, Edward Knightly, and Daniel M Mittleman. 2021. Line-of-Sight and Non-Line-of-Sight Links for Dispersive Terahertz Wireless Networks. APL Photonics 6, 4 (2021), 041304.
- [9] Yasaman Ghasempour, Rabi Shrestha, Aaron Charous, Edward Knightly, and Daniel M. Mittleman. 2020. Single-Shot Link Discovery for Terahertz Wireless Networks. Nature Communication 11, 1 (2020), 2017.
- [10] Yasaman Ghasempour, Chia-Yi Yeh, Rabi Shrestha, Yasith Amarasinghe, Daniel Mittleman, and Edward W. Knightly. 2020. LeakyTrack: Non-Coherent Single-Antenna Nodal and Environmental Mobility Tracking with a Leaky-Wave Antenna. In Proc. ACM SenSys. 56–68.
- [11] Yasaman Ghasempour, Chia-Yi Yeh, Rabi Shrestha, Daniel Mittleman, and Edward Knightly. 2020. Single Shot Single Antenna Path Discovery in THz Networks. In Proc. ACM MobiCom. 317–327.
- [12] Wei Gong and Jiangchuan Liu. 2017. Robust Indoor Wireless Localization using Sparse Recovery. In IEEE 37th International Conference on Distributed Computing Systems (ICDCS). IEEE, 847–856.
- [13] Frank B. Gross. 2011. Frontiers in Antennas: Next Generation Design & Engineering. McGraw-Hill Education.
- [14] Hichem Guerboukha, Yasith Amarasinghe, Rabi Shrestha, Angela Pizzuto, and Daniel M Mittleman. 2021. High-volume Rapid Prototyping Technique for Terahertz Metallic Metasurfaces. Optics Express 29, 9 (2021), 13806–13814.
- [15] H Guerboukha, R Shrestha, J Neronha, O Ryan, M Hornbuckle, Z Fang, and DM Mittleman. 2020. Efficient Leaky-Wave Antennas at Terahertz Frequencies Generating Highly Directional Beams. Applied Physics Letters 117, 26 (2020), 261103.
- [16] Ismail Guvenc, Chia-Chin Chong, and Fujio Watanabe. 2007. NLOS Identification and Mitigation for UWB Localization Systems. In IEEE Wireless Communications and Networking Conference. IEEE, 1571–1576.
- [17] J. Xiong and K. Jamieson. 2013. ArrayTrack: A Fine-grained Indoor Location System. In Proc. of USENIX NSDI.
- [18] David R. Jackson and Arthur A. Oliner. 2008. Leaky-Wave Antennas. Modern Antenna Handbook (2008), 325–367.
- [19] Kiran Joshi, Dinesh Bharadia, Manikanta Kotaru, and Sachin Katti. 2015. WiDeo: Fine-grained Device-Free Motion Tracing using RF backscatter. In 12th USENIX Symposium on Networked Systems Design and Implementation (NSDI). 189–204.
- [20] Nicholas J Karl, Robert W McKinney, Yasuaki Monnai, Rajind Mendis, and Daniel M Mittleman. 2015. Frequency-division Multiplexing in the Terahertz Range using a Leaky-wave Antenna. Nature Photonics 9, 11 (2015), 717.
- [21] Mohamed R Mahfouz, Cemin Zhang, Brandon C Merkl, Michael J Kuhn, and Aly E Fathy. 2008. Investigation of High-Accuracy Indoor 3-D Positioning using UWB Technology. IEEE Transactions on Microwave Theory and Techniques 56, 6 (2008), 1316–1330.
- [22] C Meier, A Terzis, and S Lindenmeier. 2007. A Robust 3D High Precision Radio Location System. In 2007 IEEE/MTT-S International Microwave Symposium. IEEE, 307–410
- [23] Rajind Mendis and Daniel Grischkowsky. 2001. Undistorted Guided-Wave Propagation of Subpicosecond Terahertz Pulses. Optics letters 26, 11 (2001), 846–848.
- [24] Rajind Mendis and Daniel M Mittleman. 2009. Comparison of the Lowest-Order Transverse-Electric (TE 1) and Transverse-Magnetic (TEM) Modes of the Parallel-Plate Waveguide for Terahertz Pulse Applications. Optics express 17, 17 (2009), 14839–14850.

- [25] Rajind Mendis and Daniel M Mittleman. 2010. A 2-D Artificial Dielectric With  $0 \le n < 1$  for the Terahertz Region. *IEEE Transactions on Microwave Theory and Techniques* 58, 7 (2010), 1993–1998.
- [26] Rajind Mendis, Abhishek Nag, Frank Chen, and Daniel M Mittleman. 2010. A Tunable Universal Terahertz Filter using Artificial Dielectrics based on Parallel-Plate Waveguides. Applied physics letters 97, 13 (2010), 131106.
- [27] Mendis, Rajind and Mittleman, Daniel M. 2009. An investigation of the Lowest-Order Transverse-Electric (TE 1) mode of the Parallel-Plate Waveguide for THz Pulse Propagation. JOSA B 26, 9 (2009), A6–A13.
- [28] Rajalakshmi Nandakumar, Vikram Iyer, and Shyamnath Gollakota. 2018. 3D Localization for Sub-Centimeter Sized Devices. In Proc. ACM SenSys. 108–119.
- [29] Ioannis Pefkianakis and Kyu-Han Kim. 2018. Accurate 3D Localization for 60 GHz Networks. In Proc. ACM SenSys. 120–131.
- 30] Sebastian Priebe, Marius Kannicht, Martin Jacob, and Thomas Kürner. 2013. Ultra Broadband Indoor Channel Measurements and Calibrated Ray Tracing Propagation Modeling at THz Frequencies. Journal of Communications and Networks 15, 6 (2013), 547–558. https://doi.org/10.1109/JCN.2013.000103
- [31] Sebastian Priebe and Thomas Kurner. 2013. Stochastic Modeling of THz Indoor Radio Channels. *IEEE Transactions on Wireless Communications* 12, 9 (2013), 4445–4455. https://doi.org/10.1109/TWC.2013.072313.121581
- [32] Kun Qian, Chenshu Wu, Zheng Yang, Chaofan Yang, and Yunhao Liu. 2016. Decimeter Level Passive Tracking with Wifi. In Proc. ACM HotWireless. 44–48.
- [33] Patrick Reynaert, Wouter Steyaert, Alexander Standaert, Dragan Simic, and Guo Kaizhe. 2017. mm-Wave and THz Circuit Design in Standard CMOS Technologies: Challenges and Opportunities. In 2017 IEEE Asia Pacific Microwave Conference (APMC). IEEE, 85–88.
- [34] Hooman Saeidi, Suresh Venkatesh, Xuyang Lu, and Kaushik Sengupta. 2021. 22.1 THz Prism: One-Shot Simultaneous Multi-Node Angular Localization Using Spectrum-to-Space Mapping with 360-to-400GHz Broadband Transceiver and Dual-Port Integrated Leaky-Wave Antennas. In 2021 IEEE International Solid-State Circuits Conference (ISSCC), Vol. 64, 314–316.
- [35] Kaushik Sengupta and Ali Hajimiri. 2012. A 0.28 THz Power-Generation and Beam-Steering Array in CMOS based on Distributed Active Radiators. IEEE Journal of Solid-State Circuits 47, 12 (2012), 3013–3031.
- [36] Li Sun, Souvik Sen, Dimitrios Koutsonikolas, and Kyu-Han Kim. 2015. WiDraw: Enabling Hands-Free Drawing in the Air on Commodity WiFi Devices. In Proc. of ACM MobiCom. 77–89.
- [37] Thang Van Nguyen, Youngmin Jeong, Hyundong Shin, and Moe Z. Win. 2015. Machine Learning for Wideband Localization. IEEE Journal on Selected Areas in Communications 33, 7 (2015), 1357–1380.
- [38] Wei Wang, Alex X Liu, and Ke Sun. 2016. Device-free Gesture Tracking using Acoustic Signals. In Proc. ACM MobiCom. 82–94.
- [39] Andreas Wille, Magdalena Broll, and Susanne Winter. 2011. Phase Difference based RFID Navigation for Medical Applications. In 2011 IEEE International Conference on RFID. IEEE, 98–105.
- [40] Dan Wu, Ruiyang Gao, Youwei Zeng, Jinyi Liu, Leye Wang, Tao Gu, and Daqing Zhang. 2020. FingerDraw: Sub-Wavelength Level Finger Motion Tracking with WiFi Signals. Proc. ACM Interact. Mob. Wearable Ubiquitous Technol. (2020).
- [41] Yaxiong Xie, Jie Xiong, Mo Li, and Kyle Jamieson. 2016. xD-Track: Leveraging Multi-Dimensional Information for Passive Wi-Fi Tracking. In Proceedings of the 3rd Workshop on Hot Topics in Wireless. 39–43.
- [42] Y. Yang, M. Mandehgar, and D. R. Grischkowsky. 2015. THz-TDS Characterization of the Digital Communication Channels of the Atmosphere and the Enabled Applications. Journal of Infrared, Millimeter, and Terahertz Waves 36, 1 (2015), 97–129.
- [43] Yihong Yang, Mahboubeh Mandehgar, and Daniel R. Grischkowsky. 2012. Understanding THz Pulse Propagation in the Atmosphere. IEEE Transactions on Terahertz Science and Technology 2, 4 (2012), 406–415.
- [44] Kegen Yu, Kai Wen, Yingbing Li, Shuai Zhang, and Kefei Zhang. 2018. A Novel NLOS Mitigation Algorithm for UWB Localization in Harsh Indoor Environments. IEEE Transactions on Vehicular Technology 68, 1 (2018), 686–699.
- [45] Ozan Yurduseven, Nuria Llombart Juan, and Andrea Neto. 2016. A Dual-Polarized Leaky Lens Antenna for Wideband Focal Plane Arrays. IEEE Transactions on Antennas and Propagation 64, 8 (2016), 3330–3337.
- [46] Faheem Zafari, Athanasios Gkelias, and Kin K Leung. 2019. A Survey of Indoor Localization Systems and Technologies. IEEE Communications Surveys & Tutorials 21, 3 (2019), 2568–2599.
- [47] Cemin Zhang, Michael J Kuhn, Brandon C Merkl, Aly E Fathy, and Mohamed R Mahfouz. 2009. Real-time Noncoherent UWB Positioning Radar with Millimeter Range Accuracy: Theory and Experiment. IEEE Transactions on Microwave Theory and Techniques 58, 1 (2009), 9–20.
- [48] Guoqiang Zhang, Haopeng Li, and Fabian Wenger. 2020. Object Detection and 3d Estimation via an FMCW Radar using a Fully Convolutional Network. In ICASSP 2020-2020 IEEE International Conference on Acoustics, Speech and Signal Processing (ICASSP). IEEE, 4487–4491.
- [49] Lingyan Zhang and Hongyu Wang. 2019. 3D-WiFi: 3D Localization With Commodity WiFi. IEEE Sensors Journal 19, 13 (2019), 5141–5152.